Use of bioresorbable fibers for short-wave infrared spectroscopy using time-domain diffuse optics

Research Article | Vol. 15, No. 9 / 1 Sep 2024 / Biomedical Optics Express 5041
Biomedical Optics EXPRESS

Use of bioresorbable fibers for short-wave infrared spectroscopy using time-domain diffuse optics

VAMSHI DAMAGATLA,[1,*] NADIA G. BOETTI,[2] LAURA DI SIENO,[1] ILARIA BARGIGIA,[1,3] FABIO NEGRETTI,[1] DIEGO PUGLIESE,[4,5] DAVIDE JANNER,[4] LORENZO SPINELLI,[6] ANDREA FARINA,[6] AND ANTONIO PIFFERI[1,6]

[1]*Politecnico di Milano, Dipartimento di Fisica, Milano, Italy*
[2]*Fondazione LINKS-Leading Innovation and Knowledge for Society, Torino, Italy*
[3]*Center for Nano Science and Technology@PoliMi, Istituto Italiano di Tecnologia, Milano, Italy*
[4]*Politecnico di Torino, Dipartimento di Scienza Applicata e Tecnologia and INSTM Research Unit, Torino, Italy*
[5]*Istituto Nazionale di Ricerca Metrologica (INRiM), Torino, Italy*
[6]*Istituto di Fotonica e Nanotecnologie, Consiglio Nazionale delle Ricerche, Milano, Italy*
[*]*saivamshi.damagatla@polimi.it*

Abstract: We demonstrate the usability of bioresorbable phosphate glass fibers for time-domain diffuse optical spectroscopy (TD-DOS) in the short-wave infrared (SWIR) region of 950–1600 nm, with the use of an InGaAs detector. Bioresorbable fibers for diffuse optics present an exciting prospect due to their ability to be left implanted while retrieving optical properties from deeper regions (few cm) for monitoring treatments. Extending TD-DOS to the SWIR region could be useful to better identify biomarkers such as water, lipids and collagen, given their increase in absorption in this range. We attempt to use the bioresorbable fibers to spectrally identify these biomarkers by measuring a series of biological samples known to contain them, such as porcine muscle, porcine fat and bone. We further validate our measurements by comparing the optical properties of high-scattering solid silicone phantoms retrieved with these bioresorbable fibers with those by a standard Si fiber.

1. Introduction

The pages of science fiction have long been filled with stories of humans with artificial additions such as life saving mechanical implants or power enhancing machine modifications. Be it Anakin and Luke Skywalker's prosthetic limbs, Mad-eye Moody's replacement eye, Wolverine's claws or the all controlling chip of the Matrix – human beings have always been fictionally fascinated by the combination of man and machine. However, historically and scientifically, some of the biggest issues with translating these ideas to the real life were not regarding the complex physics or the minuscule electronics, but rather about the bio-compatibility – a need to be non toxic to the surrounding tissue. Since the first recorded medical implantation in the 1950's [1], the medical community has come a long way utilizing these implants extensively. Following the introduction of implantable medical devices (IMDs), probably the next revolution in the field of implantable devices has been the advent of bioresorbable materials. These materials possess the quality of firstly being biocompatible, and secondly, being able to dissolve into harmless digestible components inside the human body, with a well-known example being that of surgical stitches [2]. With research progressing massively over the past decades, there have been different bioresorbable materials – silks, glasses, glass ceramics, single and polycrystals, polymers and composites [3,4].

#531681 https://doi.org/10.1364/BOE.531681
Journal © 2024 Received 3 Jun 2024; revised 8 Jul 2024; accepted 8 Jul 2024; published 5 Aug 2024

Biomedical Optics EXPRESS

Their usage for biophotonics has been possible due to the development of bioresorbable glasses which have been utilized to develop various optical elements such as photonic crystals, diffraction gratings, microlens arrays and optical fibers [5–8]. Optical bioresorbable fibers, in particular those made of calcium phosphate glasses (CPGs) [9], offer the viability to leave a fiber probe implanted to perform continuous measurements for thermal treatment, photodynamic therapy monitoring, post surgical internal monitoring, regrowth of tissues around a scaffold, etc [10–14]. With the development of specialized fibers with internal capillaries, it could also be possible to utilize the same probe for drug diffusion for treatment, thus monitoring at the same time the drug diffusion and the effect of the therapy [15]. Another key advantage is the non-toxicity and resorbability of these fibers in case of internal breakage.

Among the different photonic technologies used to retrieve information through fiber-based probes, we operate with diffuse optics, which allows retrieving information from diffuse photons travelling through the tissue at depths of few cm [16]. Since many years, the field of diffuse optics has attempted to probe the human tissue through different methodologies such as the continuous wave (CW) [17], frequency-domain (FD) [18] and time-domain (TD) [19] approaches. In particular, working with time-domain diffuse optical spectroscopy (TD-DOS), based on the detection of the distribution of time-of-flight (DTOF) of injected photons, we obtain additional advantages: (i) disentanglement of the absorption from the scattering properties; (ii) comparatively larger probed depths (in the order of a few cm) based on the TOF of the photons; (iii) insensitivity to amplitude fluctuations, which could be useful to remove effects of laser fluctuations or bleeding near the fiber tip [19,20]. Over the years there has been tremendous research in TD-DOS and it has been used for various applications such as breast imaging for screening, diagnosis and chemotherapy monitoring [21–24], functional brain monitoring [25,26], pulse oximetry, neonatal monitoring [27,28], etc. among others, and many of these techniques are currently undergoing clinical trials. While most of these techniques are based on single or multi-wavelength measurements, broadband spectroscopy is crucial in exploring new spectral regions, identifying optimal operating wavelengths and searching for novel biomarkers. Broadband spectroscopy has been utilized in TD-DOS for measurement of various samples and *in-vivo* applications [29], but has generally been limited to the therapeutic window of 600 - 1100 nm, mainly due to the limited availability of single photon detectors in the short wavelength infrared (SWIR) region. In particular, the silicon photomultipliers (SiPMs) and the single photon avalanche diodes (SPADs), which are the workhorses of the TD-DOS field [30,31], are limited by the falling efficiency of silicon beyond 900 nm. In this aspect, to go beyond this limitation could be interesting as it opens up areas to identify additional biomarkers and their wavelength ranges such as lipids and collagen which have more prominent peaks in the SWIR region [32]. Given that their absorption is much higher than in the therapeutic window, it could be easier to detect and quantify their presence [33]. It could also be useful to avoid fluorescence effects arising in the red regions. Further, scattering is decreasing upon increasing wavelength, thus deeper depth penetration could be expected, though this is counterbalanced by the significantly higher tissue absorption. Finally, also the reduced photon energy implies that a higher number of photons can be injected into the tissue for the same amount of delivered laser power. One of the key limitations has been the lack of easy access to the InGaAs array sensors, which are the most common ones used for SWIR spectroscopy. However, SWIR spectroscopy has been used for certain applications such as soil spectroscopy [34], studying the absorption spectra of biological components such as lipids, collagen using TD-DOS, etc. [35,36]; moreover, recent technological advancements have facilitated easier access to InGaAs SPADs in the field of biomedical optics, and this was another key motivation for this measurement campaign [37].

Having already tested the use of these CPG bioresorbable fibers for broadband spectroscopy in the near-infrared (NIR) region using a SiPM [38] and performed interstitial, null-separation spectroscopy utilizing a time-gated silicon SPAD [39], we wished to explore further the use of

Biomedical Optics EXPRESS

these fibers at higher wavelengths. In this paper, we demonstrate SWIR spectroscopy in the range of 950 - 1600 nm with bioresorble fibers, by coupling them to an InGaAs SPAD. After a brief description of the preparation of the fibers, we will present the experimental setup, the samples, and the analysis methods used to retrieve the optical coefficients. Then, we will compare the retrieval of the absorption and scattering spectra in a standard silicone phantom comparing bioresorbable against standard telecom fibers. Finally, we will attempt to retrieve the optical properties in the SWIR region of different biological samples including porcine meat, porcine fat, and bone.

2. Fabrication of the bioresorbable fiber

The bioresorbable optical fibers were fabricated by preform drawing utilizing the rod-in-tube technique for obtaining the preform. The core and cladding glasses were synthesized starting from high purity (99+%) chemicals (P_2O_5, CaO, MgO, Na_2O, B_2O_3, SiO_2), weighed, mixed and then melted in an alumina crucible at a temperature of 1200 °C for 1 h under a controlled atmosphere. The refractive indices of the core and cladding glasses were measured at five wavelengths – 633, 825, 1061, 1312, 1533 nm – with a Metricon 2010 prism coupler. At 633 nm the refractive indices of the core and the cladding revealed to be 1.5343 $^{\pm}$ 0.0005 and 1.5214 $^{\pm}$ 0.0005, respectively, corresponding to a fiber numerical aperture (NA) value of 0.20. The core glass was then cast into a cylindrical mold, while the cladding tube was shaped by extrusion using an in-house developed equipment. The core-cladding preform was obtained by inserting the stretched core into the cladding tube, then the optical fiber with dimensions of 200/400 μm for the core and cladding, respectively, was drawn using an in-house developed drawing tower (SAET, Turin, Italy). Finally, the quality and morphology of the fabricated optical fiber were then inspected under a Nikon ECLIPSE E 50i optical microscope. Detailed information on the bioresorbable glass and thermo-mechanical and optical properties of the fiber, as well as on dissolution studies performed in phosphate buffer saline (PBS) solution are described in other works [5,38,40].

3. Materials and methods

3.1. Experimental setup

The measurements were performed using a state-of-the-art TD-DOS setup developed at Politecnico di Milano (Fig. 1(a)) [35,41,42]. Picosecond pulses at 40 MHz from a super continuum laser (SuperK Extreme, NKT Photonics, Denmark) were spatially dispersed using a constant deviation prism and were focused and coupled into a 62/125 μm graded-index fiber, which was coupled to the samples through a variable attenuation stage. By controlling the attenuator and prism positions, we could control the input power and scan the wavelengths from 950 up to 1600 nm in steps of 5 nm. The diffuse photons were injected into and collected from the samples using the 200 μm core CPG fibers. The detection fiber was then coupled into a 62.5 μm core graded-index fiber and to the detector. The detection mechanism featured a fiber-coupled InGaAs SPAD (Micro Photon Devices S.r.l., Italy) with an active area of 25 μm which was utilized in the gated mode with a gate width of 7 ns to reduce dark noise. The gate is triggered by the laser electrical signal [43]. The photons were counted by a time-correlated single-photon counting (TCSPC) module (SPC-130, Becker and Hickl, Germany) to obtain the DTOFs.

As a first test, the instrument response function (IRF) of the CPG fiber was compared with a standard silica fiber (hereby referred to as Si fiber) with respect to three aspects as shown in Fig. 1: (i) temporal shape of the DTOF; (ii) full width at half maximum (FWHM) and (iii) temporal position of the peak of the DTOF. Figure 1(f) shows the relative, temporal position of the peaks of the two IRFs as a function of the wavelength. Apart from the change in the direction of the dispersion at the same zero-dispersion wavelength, one also notices the same trend between the

Biomedical Optics EXPRESS

two fibers regarding the temporal position of the peak, suggesting that there is no additional dispersion in the CPG fibers. Investigating further the shape of the IRF, Fig. 1(e) shows the DTOFs of the IRFs at the wavelength of 1200 nm, and we observe them to be very similar in their shape, and this is also the case at other wavelengths. On the other hand, Fig. 1(g) shows the change in FWHM with wavelength, with the FWHM staying almost constant at about ≈80 ps up to 1300 nm, and then gradually starts to increase for the wavelengths beyond. However, this is due to the broadening of the laser pulse and is evident also with the Si fibers. Further, the two fibers display a variation in FWHM of just ≈10 ps across the wavelength range. These three parameters suggest that we do not have additional dispersion or temporal broadening due to the CPG fibers and hence they function similar to a standard Si fiber with regards to the temporal profile.

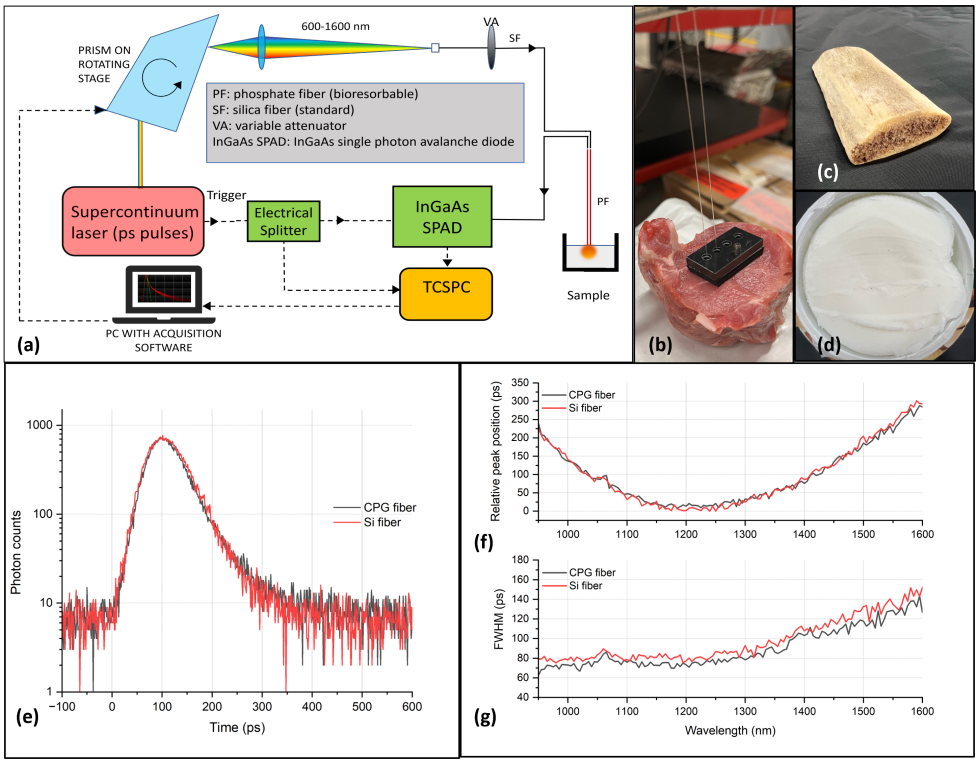

Fig. 1. (a) Schematic of the experimental setup: solid lines - optical paths, dashed lines - electrical paths. (b) Porcine muscle under measurement. (c) Processed bovine bone. (d) Processed porcine fat. (e) IRFs taken with the CPG and Si fibers at 1200 nm. (f) Change in temporal peak position with wavelength. (g) Evolution of FWHM with wavelength.

3.2. *Data analysis*

The DTOFs were analyzed using three different methods for the geometry of a semi-infinite medium – (i) Diffusion equation: with the diffusion approximation to the radiative transfer equation (ii) Monte Carlo (MC): with Monte Carlo libraries generated for the specific detection geometries (iii) Mie law (MC): with a second level fitting on the MC fitting that is referred to as 'Mie law (MC)' and will be explained in detail in the following. The first analysis was performed using the diffusion equation (DE), by utilizing its Green's function solution for a semi-infinite geometry [16]. The IRF was convolved with the analytical solution of the DE

Biomedical Optics EXPRESS

and it was fitted to the DTOF using the Levenberg-Marquadt nonlinear optimization [44] to find the best combination of μ_a and μ_s' through an inversion process. However, the DE suffers from certain problems as the approximation fails for combinations of optical properties with low scattering and high absorption. This happens to be the exact case as we go higher into the SWIR: the scattering following the Mie theory drastically reduces, while the absorption of most common biological markers such as water and lipids heavily increases [33], leading to errors in the estimation of the optical properties. Particularly, due to an overestimation of the scattering at these high absorption regions, the algorithm could tend to compensate fitting the DTOF with an analytical solution with a steeper slope, and consequently a larger absorption. This correlation between the absorption and scattering is hereon referred to as μ_a - μ_s' coupling. To circumvent this issue, we employed the use of DTOF libraries created by MC modelling to recover the optical properties. Further, as a secondary refined analysis, using the Mie scattering law, we fitted noise free region of the obtained μ_s' spectrum to obtain the scattering amplitude (a) and scattering power (b) parameters using the equation $\mu_s' = a(\lambda/\lambda_o)^{-b}$, where λ_o = 950 nm. The 'a' and 'b' parameters are related to the density and size of the scattering centers, respectively [45]. These were then used to extrapolate the reduced scattering coefficient across the wavelength range to obtain better estimates. This μ_s' was then kept as a fixed input for the secondary fitting to retrieve the μ_a using the MC libraries again. This secondary fitting method is henceforth referred to as the Mie law.

3.3. Samples

3.3.1. Silicone phantoms

To test the feasibility of absorption retrieval using these fibers, silicone phantoms with high scattering values were prepared – so as to perform an initial test while avoiding μ_a - μ_s' coupling during optical properties' retrieval (as explained in Section 3.2). Silicone elastomer Sylgard 184 (base 10 and curing agent 1, Dow Europe GmbH, Germany) was employed in the preparation of the solid phantoms. The phantoms were cylindrical with a base diameter of roughly 63 mm and a height of 40 mm. The scattering properties were obtained by addition of titanium dioxide powder (CAS: 1317-70-0, Sigma-Aldrich Chemie GmbH, Germany), whereas absorption properties were only attributable to the bulk material. Nominal values of 25 and 50 cm^{-1} of reduced scattering coefficient at 690 nm were obtained by mixing 319 and 638 mg of TiO_2 (weighing res. 0.01 mg), respectively, in 128 g of base (weighing res. 0.01 g). After manual stirring, 12.8 g of curing agent (weighing res. 0.01 g) were added, following a mass ratio of 1:10 with respect to the base and the two mixtures were then treated 3 times in a planetary centrifugal mixer (Kakuhunter SK-300SII, Shashin Kagaku, Japan) for 3 min each at 2000 rpm.

In between each centrifuge treatment, the solutions were manually homogenized to better incorporate some TiO_2 precipitated at the bottom of the container. The solutions were then poured into cylindrical Nalgene jars (2118-004, Thermo Scientific, United States) and placed under a vacuum pump (XDS5, Edwards Vacuum, Sweden) at roughly 10 kPa until air bubbles disappeared, while carefully avoiding the boiling point of the mixtures. Finally, curing was performed by placing the samples into an oven (UT 20P, Heraeus, Germany) at 65 °C for 24 h. Further information on the preparation and reproducibility of these phantoms can be found in other works [46]. The two silicone phantoms, hereby referred to as PH25 and PH50, were first measured using standard Si fibers with an inter-fiber distance of ρ = 1.3 cm to get reference spectra for the optical properties. Consequently, the Si fibers were replaced with the CPG ones for injection and collection with an inter-fiber distance of ρ = 0.9 cm to compare their performance to the standard fibers. A minor point to be noted is that, while for the conventional fibers it is straightforward to make a probe to hold them in place and accurately measure the inter-fiber distance, these CPG fibers are bare fibers without any external jacket, and have an overall diameter of 400 µm. To avoid breaking them, a probe with holes of 1 mm diameter to hold the fibers

Biomedical Optics EXPRESS

in position, was used to give them some freedom against the tension due to the fibers being vertically aligned, and also to not damage the cleave while inserting them into the probe. Thus, in the case of these measurements, while the nominal distance was calculated between the center of the probe's holes as 0.9 cm, the strain of the fibers and the smoothness of the phantom surface added an uncertainty of $^{\pm}0.1$ cm to the measured inter-fiber distance.

3.3.2. Biological phantoms

The next experiment consisted of measurements on biological samples – porcine muscle, a processed bovine bone and processed porcine fat as shown Fig. 1(b), (c) and (d), respectively. The aim of this experiment was to test the CPG fibers to retrieve the various absorption spectra as compared to literature and hence the samples were chosen so as to have predominantly just one single underlying component. While the bone sample was a processed, dehydrated bone stored in lab conditions, and was measured to obtain predominantly higher collagen content, the porcine fat was a processed, commercial fat sample and was expected to contain only lipids. The porcine muscle on the other hand was chosen due to its higher water content as compared to lipids. It must also be noted that the absorption of haemoglobin is negligible in this wavelength range and hence is not considered as primary component [32]. All the samples were measured by placing the fiber tips on the surface of the sample with a black sheet in between them to prevent leakage of direct photons along the surface. The inter-fiber distances were varied across the samples so as to select the largest ρ with the maximum signal-to-noise ratio and these details are mentioned in Table 1. The inter-fiber distances used to measure the bone, the muscle and the fat sample were 0.5, 0.9 and 1.1 cm, respectively. For the case of the bone, the fibers were placed on the inner ends of the probe holes to obtain a minimum $\rho = 0.5$ cm. However, given the 1 mm radius of the two holes, this leads to uncertainty of +0.2 cm in its measurement due to the smoothness of the sample, the tension in the fiber and the size of the probe hole. However, this uncertainty was not a problem for the other two samples as the fibers were placed with slight pressure into the surface of the muscle and fat samples, ensuring that they could not move.

4. Results and discussion

Figure 2(a) and (b) show the reduced scattering spectra of the PH25 and PH50 phantoms, respectively, while 2(c) and (d) show the corresponding absorption spectra as retrieved by the CPG fibers and compared to those obtained with the standard Si fibers. From the μ_s', we can see firstly that, due to the high scattering values, there is no cross-talk between μ_a and μ_s' leading to an increase in the scattering, and the scattering appears to follow the Mie law. Conversely, there appears to be a dip in the scattering which in fact can be attributed to the lack of signal at the absorption peaks due to the high absorption. From the absorption spectra one can clearly see the two prominent expected peaks at around 1180 and 1400 nm, along with other minor peaks below 1100 nm [47].

Figure 2(a) and (b) also contain a yellow shaded region. As explained previously, there exists an uncertainty in the position of the fibers and hence also in the retrieved reduced scattering coefficient. This region of uncertainty in μ_s' is calculated as the area between expected values for the upper and lower limits of ρ, and is shown in yellow in the graph. While the μ_s' retrieved for PH25 is similar for both the fibers, there exists a $\approx$10% variation for PH50, which however is still within the region of uncertainty and is hence acceptable. While this causes a relative error in the μ_s', the absorption retrieval is independent of this uncertainty in ρ with changes only in the third decimal point. Further, the diffusion equation and the Monte Carlo methods have some discrepancies at the absorption peak due to the $\mu_a - \mu_s'$ coupling being either positive or negative. However, by employing the Mie law correction for analysis, one observes similar values for the various absorption peaks across the fibers and phantoms. Table 1 also shows the 'a' and 'b' parameters obtained from the Mie law fitting, and as expected the scattering amplitude (b) values

Biomedical Optics EXPRESS

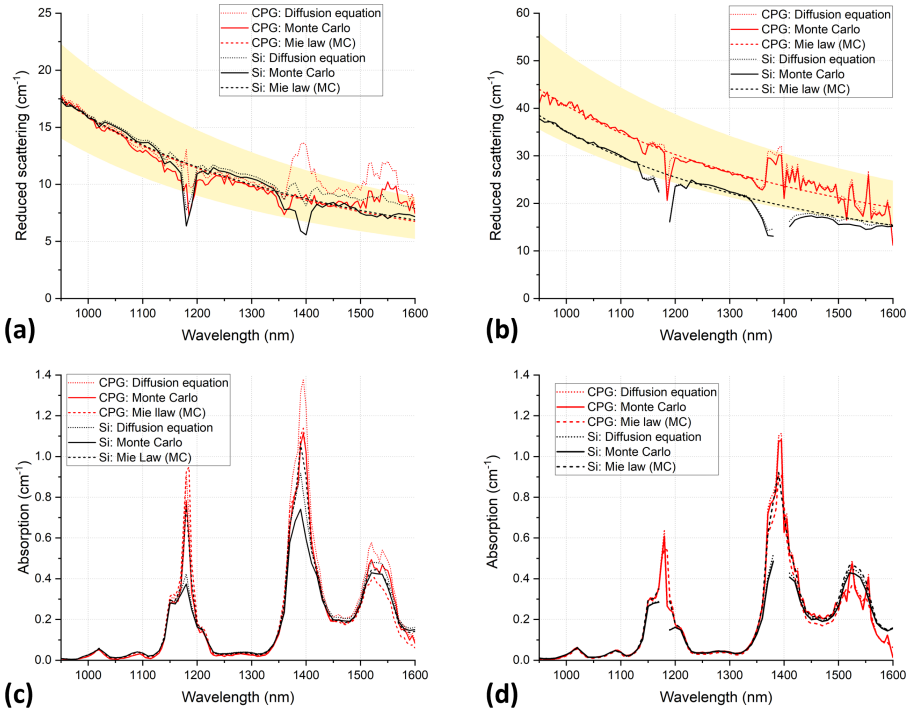

Fig. 2. Reduced scattering spectra of (a) PH25 and (b) PH50 phantoms, and absorption spectra of (c) PH25 and (d) PH50 phantoms. The yellow shaded regions in (a) and (b) depict the error in reduced scattering retrieval, due to uncertainty in the measurement of inter-fiber distance.

turn out to be similar given that they carry information on the size of the same scattering centers. Thus, the CPG fibers were able to retrieve the optical properties of the phantoms as well as the standard Si fibers within the margin of uncertainty, thus validating their use further as compared to the Si fiber.

We continued then to measure the biological phantoms. First, we measured the processed bone sample with $\rho = 0.5$ cm. Due to lack of signal, we were only able to measure it up to 1350 nm. As can be observed from Fig. 3(a), the bone shows slightly unusually high μ_s' (> 60 cm^{-1}) for most of the region and hence we observe only a tiny bit of μ_a - μ_s' coupling. However, in this case, we had an uncertainty in the fiber position of +0.2 cm due to the fibers being placed in the closer ends of the probe. Due to the small value of $\rho = 0.5$ cm, the relative error is higher and gives us an uncertainty region going down to < 40 cm^{-1}, which is more in agreement with expected values from literature. On the other hand, the absorption spectrum (Fig. 3(b)) of the bone clearly shows the underlying spectra of collagen which happens to be the primary protein and biomarker present in an ex-vivo, dehydrated and processed bone sample.

We then moved on to measure the porcine meat and fat samples. Since it is well known that the muscle and fat have a low scattering and high absorption in the SWIR region which leads to a breakdown of the diffusion approximation, we decided to omit the diffusion equation for analysis of these samples due to the presence of a large $\mu_a - \mu_s'$ coupling. Having then performed a MC fit for the muscle tissue, we utilized the analysis strategy outlined in the Section 3.2 to further smoothen the spectrum by calculating the Mie scattering parameters from the initial part of the scattering spectrum to estimate the reduced scattering. The muscle tissue indeed poses a challenge due to its extremely low scattering in this wavelength region. While it is known to

Biomedical Optics EXPRESS

have low μ_s' values [48], it is also known that the Mie law tends to flatten out with increasing wavelength. A mixture of factors such as small inter-fiber distance, flattening of the μ_s' and high absorption, added noise to fitting of the scattering. Consequently, we obtained the corrected absorption spectrum of the muscle from a secondary fitting process with the Mie constraint, which indeed matches with the water absorption spectrum shown as a reference with the peaks at 980 and 1100 nm. For both the bone and muscle samples, the spectra are depicted up to 1380 nm due to a lack of signal at higher wavelengths due to the high absorption.

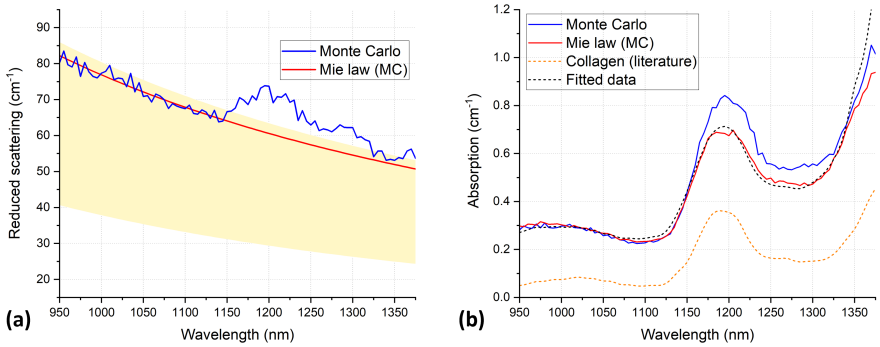

Fig. 3. (a) Reduced scattering and (b) absorption of the processed bone sample. The yellow shaded region in (a) depicts the error in reduced scattering retrieval, due to uncertainty in the measurement of inter-fiber distance.

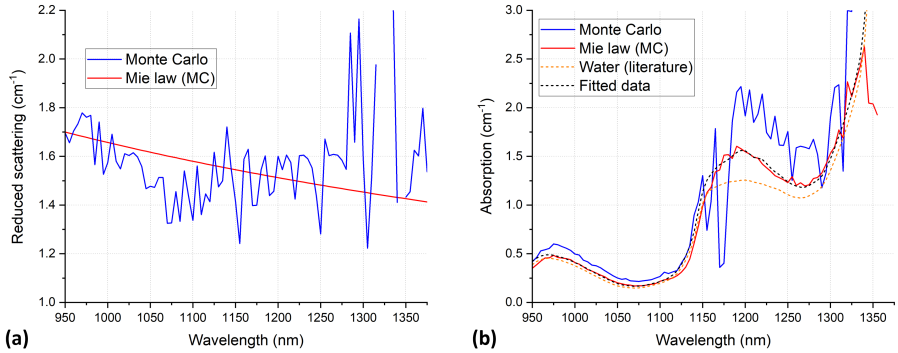

Fig. 4. (a) Reduced scattering and (b) absorption of the porcine muscle sample.

On the other hand, the porcine fat spectrum has relatively lower absorption and thus we were able to measure it up to 1600 nm. The scattering spectrum, shown is Fig. 5(a), is in line with expected values and shows a Mie law dependence, with discrepancies at wavelengths corresponding to the absorption peaks. The retrieved absorption spectra, instead, are reported in Fig. 5(b) and highlight the well documented lipid peaks at 1210 and 1400 nm.

Table 1 also shows the component analysis performed to retrieve the concentrations of the various biomarkers by fitting them with spectra of lipids, water and collagen from literature. Due to the extremely low concentrations of oxy and deoxy-haemoglobin, we have omitted them from the fitting process. As expected, the fat sample contains only lipids, whereas in the muscle sample, the concentration of water is about 10 times that of the other constituents. Similarly, more than 50% the bone is constituted by collagen. Figure 3(b), 4(b) and 5(b) also contain these fitted spectra along with the experimentally obtained spectra. Comparing the shape of fitted spectra to those from literature and taking into account the plausible relative concentrations of

Biomedical Optics EXPRESS

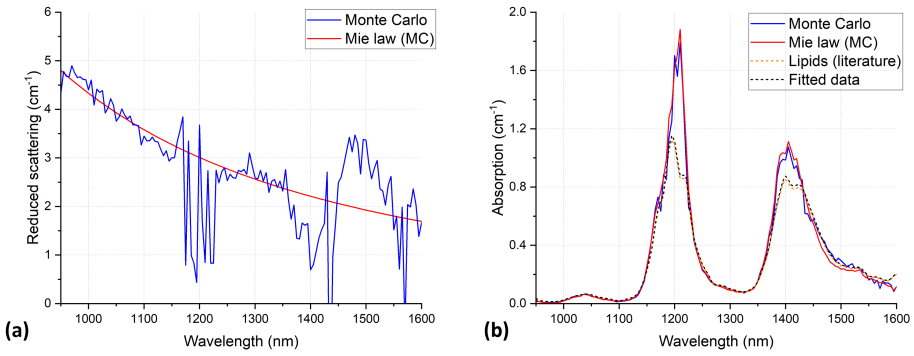

Fig. 5. (a) Reduced scattering and (b) absorption of processed porcine fat.

components, it confirmed that our choice of samples indeed had predominantly only a single component. However, it must be noted that these values are only indicative, as the reference spectra do not include haemoglobin (due to its low values) and the samples considered are either ex-vivo or processed samples.

Table 1. Comparision of 'a' and 'b' parameters from the Mie fitting, along with the fitted concentrations of underlying components.

Sample	ρ (cm)	Uncertainty in ρ (cm)	a (cm^{-1})	b	Water (mg/cm^3)	Lipids (mg/cm^3)	Collagen (mg/cm^3)
Processed bone	0.5	+ 0.2	82.20	1.306	112	40	198
Porcine muscle	0.9	-	1.70	0.501	1003	173	52
Processed fat	1.1	-	4.81	2.010	0	934	0
PH25 (CPG)	0.9	± 0.1	17.30	1.769	-	-	-
PH50 (CPG)	0.9	± 0.1	44.01	1.601	-	-	-
PH25 (Si)	1.3	-	17.50	1.790	-	-	-
PH50 (Si)	1.3	-	38.05	1.760	-	-	-

5. Conclusions

In conclusion, we were able to demonstrate the usability of bioresorbable CPG fibers in the SWIR region for TD-DOS measurements on biological samples. Bioresorbable fibers are a rapidly progressing field of interest that holds tremendous potential due to their bioresorbability capabilities. After successfully demonstrating their use in a TD-DOS setting at Vis-NIR wavelengths for standard and interstitial spectroscopy [39], this work extends their range of applicability to include the SWIR region. By utilizing an InGaAs SPAD, we were able to collect photons at higher wavelengths and retrieve the optical properties of phantoms and common *ex-vivo* tissues. We were able to demonstrate its equivalence to a standard Si fiber by measurements on silicone phantoms with high scattering values. Further we were able to retrieve the absorption and scattering spectra of biological samples – bone, muscle and fat samples. By utilizing Monte Carlo libraries for fitting with a further secondary Mie constraint on μ_s' retrieval, we were able to remove the μ_s' - μ_a coupling and obtain the corrected absorption spectrum and recognize the underlying components of collagen, water and lipids. This window could be exploited also to analyze other biomarkers such as other proteins (e.g. elastin or albumin) [49] which display a low absorption in the 600 - 1000 nm range and are overshadowed by blood components. Additionally,

Biomedical Optics EXPRESS

it could be useful to test interstitial bone monitoring, drug diffusion, thermal treatment monitoring using the water peak, etc.

Further works could be addressed to perform these measurements with a higher laser power (e.g. by using a tunable optical parametric amplifer laser) to retrieve the entire spectrum and go towards *in-vivo* studies. Another interesting direction could be to check the persistence of the probing capability of the CPG fibers over time as a function of their bioresorbability. Finally, the availability of detectors in this region has always been a bottle neck, but with the availability of reasonably affordable InGaAs SPADs in the market [43], going towards technological advances such as reduction in the background noise, increasing the count rate capacity and augmented detection area could help us in attempting interstitial null-separation spectroscopy at the SWIR wavelengths.

Funding. Horizon 2020 Framework Programme (CUP B53C22001750006, ID D2B8D520, I-PHOQS, Grant no. 860185, PHAST-ETN, CUP D53D23001030006, ID 20225MR35K, Next Generation EU - PNRR - M4C2).

Acknowledgments. The authors acknowledge infrastructural and financial support from the following sources - (i) European Union's Horizon 2020 research and innovation programme: PHAST-ETN project under the Marie Sklodowska-Curie; grant agreement No. 860185; (ii) European Union's Next Generation EU - "PNRR - M4C2, investment 1.1 - "PRIN 2022 fund" - JUNCTION ID 20225MR35K – CUP D53D23001030006; (iii) European Union's Next Generation EU Programme with the I-PHOQS Infrastructure - IR0000016, ID D2B8D520, CUP B53C22001750006.

Disclosures. The authors declare no conflict of interest.

Data availability. The dataset for all the measurements and experiments in this paper are available at [50] on the open repository ZENODO supported by OPENAIRE.

References

1. W. Greatbatch and C. F. Holmes, "History of implantable devices," IEEE Eng. Med. Biol. Mag. **10**(3), 38–41 (1991).
2. J.-M. Seitz, M. Durisin, J. Goldman, *et al.*, "Recent advances in biodegradable metals for medical sutures: a critical review," Adv. Healthcare Materials **4**(13), 1915–1936 (2015).
3. M. Prakasam, J. Locs, K. Salma-Ancane, *et al.*, "Biodegradable materials and metallic implants—a review," J. Funct. Biomater. **8**(4), 44 (2017).
4. H. Tao, J. M. Kainerstorfer, S. M. Siebert, *et al.*, "Implantable, multifunctional, bioresorbable optics," Proc. Natl. Acad. Sci. **109**(48), 19584–19589 (2012).
5. E. Ceci-Ginistrelli, D. Pugliese, N. G. Boetti, *et al.*, "Novel biocompatible and resorbable UV-transparent phosphate glass based optical fiber," Opt. Mater. Express **6**(6), 2040–2051 (2016).
6. A. Dupuis, N. Guo, Y. Gao, *et al.*, "Prospective for biodegradable microstructured optical fibers," Opt. Lett. **32**(2), 109–111 (2007).
7. N. Huby, V. Vié, A. Renault, *et al.*, "Native spider silk as a biological optical fiber," Appl. Phys. Lett. **102**(12), 123702 (2013).
8. D. Meena Narayana Menon, D. Pugliese, M. Giardino, *et al.*, "Laser-induced fabrication of micro-optics on bioresorbable calcium phosphate glass for implantable devices," Materials **16**(11), 3899 (2023).
9. D. Pugliese, N. G. Boetti, D. Janner, *et al.*, "Optical quality resorbable calcium-phosphate glasses for biophotonic applications," *Ceramics, Glass and Glass-Ceramics*, PoliTO Springer Series, (Springer, 2021).
10. A. Bossi, L. Bianchi, P. Saccomandi, *et al.*, "Optical signatures of thermal damage on ex-vivo brain, lung and heart tissues using time-domain diffuse optical spectroscopy," Biomed. Opt. Express **15**(4), 2481–2497 (2024).
11. T. Svensson, S. Andersson-Engels, M. Einarsdóttír, *et al.*, "In vivo optical characterization of human prostate tissue using near-infrared time-resolved spectroscopy," J. Biomed. Opt. **12**(1), 014022 (2007).
12. J. T. Pandayil, N. G. Boetti, and D. Janner, "Advancements in biomedical applications of calcium phosphate glass and glass-based devices—a review," J. Funct. Biomater. **15**(3), 79 (2024).
13. J. M. Dąbrowski and L. G. Arnaut, "Photodynamic therapy (PDT) of cancer: from local to systemic treatment," Photochem. Photobiol. Sci. **14**(10), 1765–1780 (2015).
14. D. Grosenick, K. Cantow, K. Arakelyan, *et al.*, "Detailing renal hemodynamics and oxygenation in rats by a combined near-infrared spectroscopy and invasive probe approach," Biomed. Opt. Express **6**(2), 309–323 (2015).
15. S. H. Mussavi Rizi, N. G. Boetti, D. Pugliese, *et al.*, "Phosphate glass-based microstructured optical fibers with hole and core for biomedical applications," Opt. Mater. **131**, 112644 (2022).
16. F. Martelli, *Light Propagation through Biological Tissue and other Diffusive Media: Theory, Solutions, and Software* (SPIE Press, 2009).
17. F. Scholkmann, S. Kleiser, A. J. Metz, *et al.*, "A review on continuous wave functional near-infrared spectroscopy and imaging instrumentation and methodology," NeuroImage **85**, 6–27 (2014).
18. S. Fantini and A. Sassaroli, "Frequency-domain techniques for cerebral and functional near-infrared spectroscopy," Front. Neurosci. **14**, 519087 (2020).

Biomedical Optics EXPRESS

19. A. Pifferi, D. Contini, A. Dalla Mora, *et al.*, "New frontiers in time-domain diffuse optics, a review," J. Biomed. Opt. **21**(9), 091310 (2016).
20. T. Durduran, R. Choe, W. B. Baker, *et al.*, "Diffuse optics for tissue monitoring and tomography," Rep. Prog. Phys. **73**(7), 076701 (2010).
21. P. Taroni, A. Pifferi, A. Torricelli, *et al.*, "In vivo absorption and scattering spectroscopy of biological tissues," Photochem. Photobiol. Sci. **2**(2), 124–129 (2003).
22. B. J. Tromberg, Z. Zhang, A. Leproux, *et al.*, "Predicting responses to neoadjuvant chemotherapy in breast cancer: ACRIN 6691 trial of diffuse optical spectroscopic imaging," Cancer Res. **76**(20), 5933–5944 (2016).
23. G. Maffeis, L. Di Sieno, A. Dalla Mora, *et al.*, "The SOLUS instrument: optical characterization of the first hand-held probe for multimodal imaging (ultrasound and multi-wavelength time-resolved diffuse optical tomography)," Opt. Lasers Eng. **176**, 108075 (2024).
24. S. Srinivasan, B. W. Pogue, S. Jiang, *et al.*, "Interpreting hemoglobin and water concentration, oxygen saturation, and scattering measured in vivo by near-infrared breast tomography," Proc. Natl. Acad. Sci. U.S.A. **100**(21), 12349–12354 (2003).
25. A. Torricelli, D. Contini, A. Pifferi, *et al.*, "Time domain functional NIRS imaging for human brain mapping," NeuroImage **85**(Part 1), 28–50 (2014).
26. A. Torricelli, D. Contini, A. Dalla Mora, *et al.*, "Neurophotonics: non-invasive optical techniques for monitoring brain functions," Functional Neurol. **29**(4), 223–230 (2014).
27. L. Spinelli, L. Zucchelli, D. Contini, *et al.*, "In vivo measure of neonate brain optical properties and hemodynamic parameters by time-domain near-infrared spectroscopy," Neurophotonics **4**(04), 1 (2017).
28. C. Amendola, L. Spinelli, D. Contini, *et al.*, "Accuracy of homogeneous models for photon diffusion in estimating neonatal cerebral hemodynamics by TD-NIRS," Biomed. Opt. Express **12**(4), 1905–1921 (2021).
29. S. Konugolu Venkata Sekar, P. Lanka, A. Farina, *et al.*, "Broadband time domain diffuse optical reflectance spectroscopy: a review of systems, methods, and applications," Appl. Sci. **9**(24), 5465 (2019).
30. A. Dalla Mora, L. Di Sieno, A. Behera, *et al.*, "The SiPM revolution in time-domain diffuse optics," Nucl. Instrum. Methods Phys. Res. Sect. A **978**, 164411 (2020).
31. A. Dalla Mora, L. Di Sieno, R. Re, *et al.*, "Time-gated single-photon detection in time-domain diffuse optics: a review," Appl. Sci. **10**(3), 1101 (2020).
32. R. H. Wilson, K. P. Nadeau, F. B. Jaworski, *et al.*, "Review of short-wave infrared spectroscopy and imaging methods for biological tissue characterization," J. Biomed. Opt. **20**(3), 030901 (2015).
33. R. Nachabé, B. H. Hendriks, M. van der Voort, *et al.*, "Estimation of biological chromophores using diffuse optical spectroscopy: benefit of extending the uv-vis wavelength range to include 1000 to 1600 nm," Biomed. Opt. Express **1**(5), 1432–1442 (2010).
34. D. J. Brown, K. D. Shepherd, M. G. Walsh, *et al.*, "Global soil characterization with VNIR diffuse reflectance spectroscopy," Geoderma **132**(3-4), 273–290 (2006).
35. I. Bargigia, A. Tosi, A. B. Shehata, *et al.*, "Time-resolved diffuse optical spectroscopy up to 1700 nm by means of a time-gated InGaAa/InP single-photon avalanche diode," Appl. Spectrosc. **66**(8), 944–950 (2012).
36. V. Sanathana Konugolu Sekar, I. Bargigia, A. Dalla Mora, *et al.*, "Diffuse optical characterization of collagen absorption from 500 to 1700 nm," J. Biomed. Opt. **22**(1), 015006 (2017).
37. A. Tosi, A. Dalla Mora, F. Zappa, *et al.*, "Ingaas/inp single-photon avalanche diodes show low dark counts and require moderate cooling," in *Quantum Sensing and Nanophotonic Devices VI*, vol. 7222 (SPIE, 2009), pp. 426–434.
38. L. Di Sieno, N. G. Boetti, A. Dalla Mora, *et al.*, "Towards the use of bioresorbable fibers in time-domain diffuse optics," J. Biophotonics **11**(1), e201600275 (2018).
39. V. Damagatla, N. G. Boetti, L. Di Sieno, *et al.*, "Use of bioresorbable fibers for interstitial time-domain diffuse optical spectroscopy with fast gating," in *Diffuse Optical Spectroscopy and Imaging IX*, (Society of Photo-Optical Instrumentation Engineers, 2023).
40. V. M. Sglavo, D. Pugliese, F. Sartori, *et al.*, "Mechanical properties of resorbable calcium-phosphate glass optical fiber and capillaries," J. Alloys Compd. **778**, 410–417 (2019).
41. S. Konugolu Venkata Sekar, A. Dalla Mora, I. Bargigia, *et al.*, "Broadband (600–1350 nm) time-resolved diffuse optical spectrometer for clinical use," IEEE J. Sel. Top. Quantum Electron. **22**(3), 406–414 (2016).
42. V. Damagatla, P. Lanka, A. Brodu, *et al.*, "Interstitial null-distance time-domain diffuse optical spectroscopy using a superconducting nanowire detector," J. Biomed. Opt. **28**(12), 121202 (2023).
43. F. Signorelli, F. Telesca, E. Conca, *et al.*, "Low-noise ingaas/inp single-photon avalanche diodes for fiber-based and free-space applications," IEEE J. Sel. Top. Quantum Electron. **28**(2: Optical Detectors), 1–10 (2022).
44. W. H. Press, S. A. Teukolsky, W. T. Vetterling, *et al.*, *Numerical Recipes 3rd Edition: The Art of Scientific Computing* (Cambridge University Press, 2007).
45. G. Maffeis, E. Ferocino, A. Dalla Mora, *et al.*, "In vivo test-driven upgrade of a time domain multi-wavelength optical mammograph," Biomed. Opt. Express **12**(2), 1105–1122 (2021).
46. F. Zhao, P. Levoni, L. Frabasile, *et al.*, "Reproducibility of identical solid phantoms," J. Biomed. Opt. **27**(07), 074713 (2022).
47. A. Agrawal, M. Connors, A. Beylin, *et al.*, "Characterizing the point spread function of retinal OCT devices with a model eye-based phantom," Biomed. Opt. Express **3**(5), 1116 (2012).

Biomedical Optics EXPRESS

48. S. Mosca, P. Lanka, N. Stone, *et al.*, "Optical characterization of porcine tissues from various organs in the 650–1100 nm range using time-domain diffuse spectroscopy," Biomed. Opt. Express **11**(3), 1697–1706 (2020).
49. S. Konugolu Venkata Sekar, J. S. Beh, A. Farina, *et al.*, "Broadband diffuse optical characterization of elastin for biomedical applications," Biophys. Chem. **229**, 130–134 (2017).
50. V. Damagatla, N. G. Boetti, L. di Sieno, *et al.*, "Use of bioresorbable fibers for short-wave infrared spectroscopy using time-domain diffuse optics: data," Zenodo, 2023, 10.5281/zenodo.12667650